LES on unstructured deforming meshes: towards reciprocating IC engines

By D. C. Haworth[1] AND K. Jansen[2]

A variable explicit/implicit characteristics-based advection scheme that is second-order accurate in space and time has been developed recently for unstructured deforming meshes (O'Rourke & Sahota 1996a). To explore the suitability of this methodology for large-eddy simulation (LES), three subgrid-scale turbulence models have been implemented in the CHAD CFD code (O'Rourke & Sahota 1996b): a constant-coefficient Smagorinsky model, a dynamic Smagorinsky model for flows having one or more directions of statistical homogeneity, and a Lagrangian dynamic Smagorinsky model for flows having no spatial or temporal homogeneity (Meneveau *et al.* 1996). Computations have been made for three canonical flows, progressing towards the intended application of in-cylinder flow in a reciprocating engine. Grid sizes were selected to be comparable to the coarsest meshes used in earlier spectral LES studies. Quantitative results are reported for decaying homogeneous isotropic turbulence, for linear (non-solenoidal) strain of homogeneous isotropic turbulence, and for a planar channel flow. Computations are compared to experimental measurements, to direct-numerical simulation (DNS) data, and to rapid-distortion theory (RDT) where appropriate. Generally satisfactory evolution of first and second moments is found on these coarse meshes; deviations are attributed to insufficient mesh resolution. Issues include mesh resolution and computational requirements for a specified level of accuracy, analytic characterization of the filtering implied by the numerical method, wall treatment, and inflow boundary conditions. To resolve these issues, finer-mesh simulations and computations of a simplified axisymmetric reciprocating piston-cylinder assembly are in progress.

1. Introduction

Contemporary three-dimensional time-dependent models for flow and combustion in reciprocating IC engines are based on solutions to Reynolds-averaged governing equations ('RANS' based modeling; Amsden *et al.* 1989, Haworth *et al.* 1990). In RANS, the local instantaneous value of a computed dependent variable represents an ensemble- or phase-average over many engine cycles at a specified spatial location and crank phasing. In general, two-equation ($k-\epsilon$) closures have been used to model turbulent transport, with standard equilibrium wall functions. Shortcomings of RANS models have been documented by several generations of turbulence

1 GM R&D Center

2 Center for Turbulence Research, currently at: Rensselaer Polytechnic Institute

researchers. Discussion of engine-specific issues can be found in the reviews by El Tahry & Haworth (1992, 1996).

An alternative to RANS is large-eddy simulation (LES). Here the governing equations are spatially filtered rather than ensemble averaged. Explicit account is taken of flow structures larger than the filter width, which is on the order of the mesh spacing, while the influence of unresolved scales is modeled using a subgrid-scale (SGS) model. Because statistics of small-scale turbulence are expected to be more universal than those of the large scales, LES offers the promise of wider generality and reduced modeling uncertainty.

LES is particularly appealing for IC engine applications. Turbulence model formulation and calibration traditionally have been carried out in statistically stationary and/or homogeneous flows for simple geometric configurations. To bring these models to bear in a phase-averaged formulation implies an equivalence between ensemble- and spatial- or temporal-averages (ergodicity) that has been demonstrated neither experimentally nor analytically. Use of conventional models also demands a reasonable degree of commonality in turbulence structure between the benchmark flow and the engine. While universality has been argued in the limit of fully-developed high-Reynolds-number broad-inertial-range turbulence, it is dubious for the low Reynolds numbers (Section 4) and complex three-dimensional transient flows that characterize the engine.

The same moderate Reynolds numbers that make IC engine flow problematic for RANS render it an appealing candidate for LES. It has been estimated that grid-independent (to a 10%-20% level) RANS computations of in-cylinder flow and combustion require at least 100^3 mesh points using second-order or higher numerical methods. This corresponds to sub-millimeter mesh spacings in a typical automotive IC engine, and is not far beyond current practice of 250,000 to 500,000 nodes. This mesh density should suffice to capture large- and intermediate-scale flow structures. Thus for IC engines, LES mesh requirements are expected to be comparable to those of RANS.

LES also promises more direct access to physical processes. Cycle-to-cycle variability in flow and combustion is one phenomenon that has proven elusive to ensemble-mean modeling and analysis. The result has been a number of largely ad hoc attempts to distinguish among 'mean,' 'turbulence,' and 'cyclic variability' components of the flow (El Tahry & Haworth 1992). This distinction becomes moot in a spatially-filtered formulation.

A drawback of LES is that substantially more computational effort may be required compared to RANS. In the engine, for example, accumulating ensemble-mean statistics via LES requires computations through multiple engine cycles. Other issues include geometric complexity (moving piston and valves) and the relatively immature state of LES for modeling complex engineering flows. It is the purpose of the present research to advance LES on several of these fronts. First, we seek to establish the limitations and resolution requirements of a particular numerical methodology (Section 2). Second, we implement and evaluate the performance of state-of-the-art subgrid-scale turbulence models on unstructured deforming meshes

(Section 3). And third, we consider several other physical modeling issues that arise in engines, including treatment of solid walls and inflow/outflow boundaries (Section 4).

2. Numerical methodology

The high-order finite difference schemes and spectral methods that traditionally have been used for DNS and LES are not suited to complex geometric configurations with moving boundaries. On the other hand, the first-order time, second-order space discretizations typically employed for engineering RANS computations (Amsden *et al.* 1989, Haworth *et al.* 1990) are overly dissipative for LES. Here we require both that the numerical methodology be compatible with the intended application of in-cylinder flow and combustion, and that it be sufficiently accurate for meaningful large-eddy simulation.

A novel discretization scheme called NO-UTOPIA (NOde-Centered Unstructured TOpology, Parallel Implicit Advection) has been developed recently by O'Rourke & Sahota (1996a, 1996b). NO-UTOPIA is a variable explicit/implicit advection scheme that differences along characteristic directions to yield formal second-order accuracy in space and time, provided that the material-speed Courant number is less than unity. It has been implemented using node-centered variables and an edge-based data structure, allowing fully unstructured meshes.

For the present study, the equations solved are those of conservation of mass, momentum, and enthalpy; the equation of state is that of an ideal gas with constant specific heats. Computations are compressible, although the Mach number is small for all cases considered here. To accommodate arbitrary mesh deformation, advective terms in the governing equations are written using velocities relative to the moving grid. A pressure-based iterative solution procedure patterned after SIMPLE is used.

The momentum equation for a control volume is obtained by integrating the Navier-Stokes equations over an arbitrary volume V with bounding surface S that is moving with velocity $\underline{v}$. Density, Cartesian velocity components, and pressure are denoted by ρ, u_i, and p, respectively; the (constant) laminar viscosity is μ_{L}. Adopting Cartesian tensor notation with summation over repeated lower-case Roman indices, the momentum equation has the form,

$$\frac{d}{dt}\int_V \rho u_i d\tau + \int_S \rho u_i (u_j - v_j) dA_j = -\int_S p dA_i + \int_S \tau_{\mathrm{eff}\,ji} dA_j + \int_V \rho g_i d\tau \ . \quad (1)$$

Here g_i is a body force per unit mass. The effective stress $\tau_{\mathrm{eff}\,ji}$ is the sum of a viscous or laminar stress $\tau_{\mathrm{L}\,ji}$ and the subgrid-scale stress $\tau_{\mathrm{SGS}\,ji}$,

$$\tau_{\mathrm{eff}\,ji} = \tau_{\mathrm{L}\,ji} + \tau_{\mathrm{SGS}\,ji} \ , \ \text{with } \tau_{\mathrm{L}\,ji} = 2\mu_{\mathrm{L}} S_{ji} - 2\mu_{\mathrm{L}} \frac{\partial u_l}{\partial x_l}\delta_{ji}/3 \ . \quad (2)$$

Here S_{ji} is the rate-of-strain tensor, $Sji = \left(\frac{\partial u_j}{\partial x_i} + \frac{\partial u_i}{\partial x_j}\right)/2$, and δ_{ji} is Kronecker's delta. No supplementary turbulence model transport equations are carried for the subgrid-scale models considered here (Section 3).

Care is needed in the specification of initial conditions. For each flow, we select a reference velocity and length U_0 and L_0 (Section 4). Fluid properties $\gamma = c_p/c_v$ (ratio of specific heats) and R (specific gas constant) are set to nominal values for air. The Mach number based on U_0 is $M_0 = U_0/c_0$ where $c_0^2 = \gamma R T_0$ is the square of the reference sound speed and T_0 the reference temperature. Reference density and pressure are ρ_0 and p_0, respectively. Laminar viscosity $\mu_{\rm L}$ is set to match the desired reference Reynolds number Re_0. Remaining reference quantities and fluid properties are specified as:

$$\begin{aligned} \gamma = 1.4 \ , \ R = 288.291 \ \mathrm{J/kg-K} \ , \ M_0 = 0.1 \ , \\ \rho_0 = 1.0 \ , \ \ p_0 = (\gamma M_0^2)^{-1} \ , \ \mu_{\rm L} = \rho_0 U_0 L_0 Re_0^{-1} \ . \end{aligned} \tag{3}$$

Initial nodal velocities and pressures are prescribed, and nodal temperatures are set such that the initial entropy is uniform, $T = T_0(p/p_0)^{(\gamma-1)/\gamma}$.

3. Subgrid-scale models

The three models considered are of the Smagorinsky type. Here the influence of unresolved (subgrid-scale) motions on the resolved scales is treated as an additional viscosity, so that $\tau_{{\rm SGS}\ ji}$ has a form identical to that of $\tau_{{\rm L}\ ji}$,

$$\tau_{{\rm SGS}\ ji} = 2\mu_{\rm SGS} S_{ji} - 2\mu_{\rm SGS} \frac{\partial u_l}{\partial x_l} \delta_{ji}/3 \ . \tag{4}$$

The subgrid-scale viscosity $\mu_{\rm SGS}$ is taken to be proportional to a norm of the local rate-of-strain $|S|$ and to a filter width Δ,

$$\mu_{\rm SGS} = \rho C_s \Delta^2 |S| \ , \ \text{with} \ |S| \equiv 2(S_{ij}S_{ij})^{1/2} \ . \tag{5}$$

The single model coefficient is C_s. It is the specification of C_s and Δ that distinguishes the three models.

3.1 Constant-coefficient Smagorinsky model

The simplest model results from taking C_s to be a constant and Δ to be equal to the mesh spacing. To accommodate non-uniform mesh spacing, Δ in Eq. (5) is specified as,

$$\Delta = V^{1/3} \ , \tag{6}$$

where V is the volume associated with a computational element.

Calibration with respect to benchmark turbulent flows has led modelers to adopt different values of C_s. For homogeneous isotropic decaying turbulence, the value $C_s = 0.17^2$ is found to result in a good match with the measurements of Comte-Bellot & Corrsin (1971) (Section 4.1). For planar channel flow, a value of $C_s = 0.1^2$ yields better agreement with measurements and DNS data (Section 4.3). The non-universality of C_s motivates the need for a more general model.

3.2 Dynamic Smagorinsky model

Germano *et al.* (1991) proposed an approach for evaluating subgrid-scale model coefficients from information contained in the resolved fields. Two filter widths are introduced, $\overline{\Delta}$ and $\widehat{\Delta}$, where $\widehat{\Delta} > \overline{\Delta}$. Dependent variables filtered at scale $\overline{\Delta}$ are denoted by the overbar notation $\overline{()}$ while the hat notation $\widehat{()}$ denotes filtering at the larger scale. Formally, the first filter corresponds to an explicit filtering of the governing equations at the scale $\overline{\Delta}$. In practice, the first filter is implicit in the numerical method. That is, the quantity $\overline{u}_i(\underline{x}, t)$ denotes the computed velocity delivered by the numerical method at position $\underline{x}$ and time t.

The second filter, or 'test filter,' corresponds to a hypothetical second filtering at a larger scale. Thus $\widehat{\overline{u}}_i(\underline{x}, t)$ represents the LES-computed velocity field filtered at scale $\widehat{\overline{\Delta}}$. Stress tensors τ_{ji} and T_{ji} represent the subgrid-scale stresses for the two filter widths, respectively: $\tau_{ji} \equiv \rho\overline{u_j u_i} - \rho\overline{u}_j\overline{u}_i$, and $T_{ji} \equiv \rho\widehat{\overline{u_j u_i}} - \rho\widehat{\overline{u}}_j\widehat{\overline{u}}_i$. Here the fluid density ρ can vary in time, but is nearly uniform in space (low Mach number). Filtering τ_{ji} through the second filter yields the quantity $\widehat{\tau}_{ji} = \rho\widehat{\overline{u_j u_i}} - \rho\widehat{\overline{u}_j\overline{u}_i}$. Then subtracting $\widehat{\tau}_{ji}$ from T_{ji} yields a second-order tensor L_{ji}, which can be thought of as the stresses resulting from turbulent motions at scales intermediate between $\overline{\Delta}$ and $\widehat{\overline{\Delta}}$:

$$L_{ji} = T_{ji} - \widehat{\tau}_{ji} = \rho\widehat{\overline{u}_j\overline{u}_i} - \rho\widehat{\overline{u}}_j\widehat{\overline{u}}_i \ . \tag{7}$$

Equation (7) is the Germano identity.

In the Smagorinsky model, subgrid-scale stresses at both scales are modeled consistently as,

$$\tau_{ji} = 2\rho C_s\overline{\Delta}^2|\overline{S}|\overline{S}_{ji} \ , \text{ and } T_{ji} = 2\rho C_s\widehat{\overline{\Delta}}^2|\widehat{\overline{S}}|\widehat{\overline{S}}_{ji} \ . \tag{8}$$

Equation (8) is substituted into Eq. (7) to yield,

$$L_{ji} = 2\rho C_s\widehat{\overline{\Delta}}^2|\widehat{\overline{S}}|\widehat{\overline{S}}_{ji} - 2\rho\widehat{C_s\overline{\Delta}^2|\overline{S}|\overline{S}_{ji}} \ . \tag{9}$$

Under the assumption that C_s and $\overline{\Delta}$ are constants with respect to the second (test) filtering operation,

$$L_{ji} = 2\rho C_s\overline{\Delta}^2\left(\left(\widehat{\overline{\Delta}}/\overline{\Delta}\right)^2|\widehat{\overline{S}}|\widehat{\overline{S}}_{ji} - \widehat{|\overline{S}|\overline{S}_{ji}} \right) = -2\rho C_s\overline{\Delta}^2 M_{ji} \ . \tag{10}$$

Equation (10) defines the second-order tensor M_{ji} which, like L_{ji}, is directly computable from the LES resolved velocity field.

The quantity $C_s\overline{\Delta}^2$ is chosen in a manner that minimizes the error in satisfying Eq. (10), $e_{ji} \equiv L_{ji} + 2C_s\overline{\Delta}^2 M_{ji}$. Here we follow Lilly (1992) in minimizing this error in a least-squares sense with the constraint that $C_s\overline{\Delta}^2$ does not vary over homogeneous directions to yield,

$$C_s\overline{\Delta}^2 = \frac{\langle L_{ij}M_{ij}\rangle}{2\langle M_{kl}M_{kl}\rangle} \ . \tag{11}$$

The angled brackets $\langle\ \rangle$ represent an average over homogeneous directions.

The dynamic model offers several advantages compared to the constant-coefficient model. Subgrid-scale viscosity increases locally in areas of low grid resolution in response to the high energy found between the two filter scales (large L_{ji}). And, μ_{SGS} decreases to zero in case all scales of motion are fully resolved locally ($L_{ji} \to 0$). A second advantage of the model as formulated here is that the filter width itself $\overline{\Delta}$ need not be explicitly specified. It is the ratio of the filter widths $\widehat{\overline{\Delta}}/\overline{\Delta}$ that appears in M_{ij} (Eq. 10). It is expected that the ratio of filter widths should be more uniform than the filter width itself on nonuniform deforming meshes.

A fundamental limitation of the model as outlined here is that it requires at least one direction of statistical homogeneity. We therefore consider a third variant of the Smagorinsky model that addresses this shortcoming.

3.3 Lagrangian dynamic Smagorinsky model

Meneveau *et al.* (1996) proposed to accumulate the averages required in the dynamic model over flow pathlines rather than over directions of statistical homogeneity. In this case, the error incurred by substituting the Smagorinsky model (Eq. 8) into the Germano identity (Eq. 7) is minimized along fluid-particle trajectories. The error to be minimized is the accumulated local squared error E along the pathline followed by the fluid particle that is located at position $\underline{x}$ at time t: $E = \int_{-\infty}^{t} e_{ij}\big(\underline{z}(t'),t'\big)e_{ij}\big(\underline{z}(t'),t'\big)W(t-t')dt'$, where $\underline{z}(t') = \underline{x} - \int_{t'}^{t} \overline{\underline{u}}\big(\underline{z}(t''),t''\big)dt''$ is the trajectory followed by the fluid particle at times $t' < t$. The quantity $W(t-t')$ is a weighting function that determines the relative importance of past events, and the error e_{ij} is the difference between left- and right-hand sides of Eq. (10). As in the previous formulation (Section 3.2), it is assumed that $C_s\overline{\Delta}^2$ does not vary strongly over the scale of the test filter. Then the value of $C_s\overline{\Delta}^2$ that minimizes the error E is,

$$C_s\overline{\Delta}^2 = \frac{\mathcal{I}_{LM}}{\mathcal{I}_{MM}}\ , \tag{12}$$

where,

$$\begin{aligned} \mathcal{I}_{LM}(\underline{x},t) &= \int_{-\infty}^{t} L_{ij}M_{ij}\big(\underline{z}(t'),t\big),t')W(t-t')dt'\ , \\ \mathcal{I}_{MM}(\underline{x},t) &= \int_{-\infty}^{t} M_{ij}M_{ij}\big(\underline{z}(t'),t\big),t')W(t-t')dt'\ . \end{aligned} \tag{13}$$

An expedient choice of weighting function is one that decays exponentially backwards in time, $W(t-t') = T^{-1}\exp[-(t-t')/T]$, T being a memory or relaxation time scale. This choice allows the integral quantities $\mathcal{I}_{LM}$ and $\mathcal{I}_{MM}$ to be expressed as solutions to transport-relaxation equations. Meneveau *et al.* (1996) observed that high numerical accuracy is not needed in the solutions of these equations, and adopted the expedient of updating nodal values of $\mathcal{I}_{LM}$ and $\mathcal{I}_{MM}$ by interpolating

from surrounding nodes at the upstream position:

$$\begin{aligned} \mathcal{I}_{LM}^{n+1}(\underline{x}) &= \max\Big(0\ ,\ a[L_{ij}M_{ij}]^{n+1}(\underline{x}) + (1-a)\mathcal{I}_{LM}^{n}(\underline{x} - \overline{\underline{u}}^{n}\Delta t) \Big)\ , \text{ and} \\ \mathcal{I}_{MM}^{n+1}(\underline{x}) &= a[M_{ij}M_{ij}]^{n+1}(\underline{x}) + (1-a)\mathcal{I}_{MM}^{n}(\underline{x} - \overline{\underline{u}}^{n}\Delta t)\ , \end{aligned} \tag{14}$$

where $a = (\Delta t/T^n)/(1 + \Delta t/T^n)$. Here superscript $n+1$ denotes quantities evaluated at the current time, superscript n quantities at the previous time, and Δt is the computational time step. Trilinear interpolation is used to evaluate quantities at the upstream position $\underline{x} - \overline{\underline{u}}\Delta t$ from computed values at the surrounding nodes.

We adopt the relaxation time T selected by Meneveau *et al.* (1996),

$$T = \theta\overline{\Delta}[\ (2\overline{\Delta}^2)^3\mathcal{I}_{LM}\mathcal{I}_{MM}\ ]^{-1/8}\ , \tag{15}$$

where the value of the model coefficient is $\theta = 1.5$. This choice for T tends to reduce the memory time in regions of high strain (large $M_{ij}M_{ij}$) and in regions of large nonlinear energy transfer (large $L_{ij}M_{ij}$). The memory time increases to reach back further in time along the particle's trajectory in case $L_{ij}M_{ij}$ remains negative over a persistent period. Negative $L_{ij}M_{ij}$ might otherwise result in negative subgrid-scale viscosity, implying energy transfer from small to large scales and numerical instability.

4. Flow configurations

In a reciprocating engine, all flow velocities scale with the mean piston speed, which is proportional to the crankshaft rotational speed; length scales are independent of engine speed. Thus the mean-flow Reynolds number Re_b (based on bore diameter and mean piston speed) and the turbulence Reynolds number Re_l (based on turbulence intensity and integral length scale) increase in proportion to engine speed. At 2,000 r/min, these are estimated to be $Re_b \approx 36{,}000$ and $Re_l \approx 1{,}000$, respectively. In-cylinder turbulence, particularly at low engine speeds, is a low-to-moderate Reynolds number phenomenon.

The number of turbulence 'eddy-turnover' times available for the decay of induction-generated turbulence in the engine is estimated to be greater than ten. Induction-generated turbulence has largely decayed by the time of ignition: it is the breakdown of the large-scale induction-generated flow structure that has the major influence on near-TDC turbulence and flame propagation. During compression and expansion, the in-cylinder flow is subjected to linear mean strains. The mean strain due to piston motion is slow compared to turbulence time scales, but persists for a large number of eddy-turnover times. These observations guide our choice of test cases for LES.

4.1 Decay of homogeneous isotropic turbulence

This canonical configuration is of relevance to the engine by virtue of the long times available for turbulence decay between intake-valve closure and ignition. Benchmark measurements were reported by Comte-Bellot & Corrsin (1971). There

the temporal decay of homogeneous isotropic turbulence was approximated by grid-generated turbulence in a wind tunnel.

Here we compare computed turbulence kinetic energy decay $\overline{k} = \langle \overline{u}_i \overline{u}_i \rangle / 2$ and three-dimensional energy spectra to the experimental data of Comte-Bellot & Corrsin (1971). Turbulence was generated using a grid spacing of $M = 5.08$ cm in a uniform mean flow of velocity $U_\infty = 10$ m/s, yielding a Reynolds number of $U_\infty M/\nu = 34{,}000$. Data were reported at three downstream stations: $U_\infty t/M = 42$, 98, and 171.

Computations are done on triply-periodic uniform cubic meshes of length 2π along each edge. Scalings are such that the edge of the computational box 2π corresponds to a physical length of 0.55 m, and the computational reference velocity $U_0 = 1.0$ corresponds to the physical velocity $U_\infty = 10.0$ m/s. Other scalings and parameters are summarized in Eq. (3).

The initial velocity field is prescribed by a procedure similar to that used for incompressible spectral simulations. We begin with a superposition of Fourier modes having a prescribed energy spectrum but random phases; this is projected onto the divergence-free space. The resulting field represents the flow upstream of the first measurement station. It is advanced in time over several turbulence eddy turnover times to adjust to compressibility and to build phase coherence. The process is repeated with different initial fields until a satisfactory match is obtained between the computed and measured energy spectrum at the first measurement station $U_\infty t/M = 42$.

Comparisons between model and measurement are made on the basis of filtered quantities. Energy spectra are filtered based on our limited understanding of the nature of the filtering implied by the numerical method. We assume that $\overline{()}$ corresponds to a top-hat filter in physical space at the mesh spacing with trapezoidal-rule integration.

Initial computations are for a mesh of 32^3 nodes. This has been the traditional starting point for new numerical methodologies in LES, but is marginal for resolving the physics of the flow. At the initial measurement station $U_\infty t/M = 42$, the computational box edge corresponds to between ten and twenty integral length scales of the turbulence: fewer than three mesh points span an integral scale. By the final measurement station $U_\infty t/M = 171$, the turbulence integral scale has roughly doubled. The computational time step is prescribed such that material Courant numbers are less than unity.

4.2 Linear strain of initially isotropic turbulence

Homogeneous strain of initially homogeneous isotropic turbulence has been a second canonical configuration for analysis, modeling, and experiment. Here we consider the linear expansion and the linear compression for their particular relevance to the IC engine. Results are compared to rapid-distortion theory (RDT), a linearized theory of turbulence that is appropriate in the limit where the mean strain rate is large compared to an inverse turbulence eddy turnover time (Kassinos & Reynolds 1994). Although IC engines appear to be far from the RDT limit, this nonetheless provides a sound basis for model evaluation. This configuration also

exercises the code's mesh deformation capability.

The behavior that we seek to capture is the distribution of energy among the three normal-stress components. We monitor the evolution of the normalized anisotropy tensor $\overline{b}_{ij}$ as a function of the total strain C^*,

$$\overline{b}_{ij} = \langle \overline{u}_i \overline{u}_j \rangle / \langle \overline{u}_l \overline{u}_l \rangle - \delta_{ij}/3 \quad , \quad C^* = \exp[\int |S^*| dt \ ] \ . \tag{16}$$

Here S^* is the dominant eigenvalue of the modified rate-of-strain tensor S^*_{ij}, where $S^*_{ij} = S_{ij} - S_{ll}\delta_{ij}/3$. In the absence of mean rotation, the evolution of $\overline{b}_{ij}(C^*)$ in the RDT limit for a non-solenoidal mean strain S_{ij} is the same as the evolution of $\overline{b}_{ij}(C^*)$ for the corresponding divergence-free rate-of-strain S^*_{ij} (Kassinos & Reynolds 1994).

The linear expansion is the superposition of spherical (isotropic) expansion and irrotational axisymmetric contraction. Experiments (see Kassinos & Reynolds 1994 for references) show that the anisotropy $\overline{b}_{ij}$ depends weakly on the magnitude of the mean rate of strain. Thus even for slow linear expansions, the evolution of $\overline{b}_{ij}(C^*)$ is expected to be similar to that predicted by RDT. The linear compression is the superposition of spherical compression and irrotational axisymmetric expansion. In this case, experiments reveal that stronger anisotropy develops at slower mean rates of strain.

Initial meshes and velocity fields are the same as those for decaying turbulence simulations (Section 4.1). The mean strain rate is imposed by deforming the domain in a manner that maintains a constant rate-of-strain S_{33} along the x_3 coordinate direction. The mesh deformation rate varies linearly from zero at $x_3 = 0$ to $S_{33} \cdot L_3(t)$ at $x_3 = L_3(t)$, yielding exponential expansion or contraction of the mesh with time, $L_3(t) = L_3(0) \cdot \exp[S_{33}t]$.

4.3 Planar channel flow

The planar channel flow adds the complexity of walls and a single statistically nonhomogeneous direction. Computations are performed on a rectangular prism of dimension L_1 (streamwise) by L_2 (normal to the wall) by L_3. Relevant dimensionless parameters are Reynolds numbers based on the wall friction velocity u_τ, and on the bulk velocity: $Re_\tau \equiv u_\tau \delta/\nu$, and $Re_B \equiv U_B \delta/\nu$ where $U_B = \int_0^{L_2} \langle \overline{u}_1(x_2) \rangle dx_2/L_2$, and δ is the channel half-width. Here angled brackets $\langle \ \rangle$ denote averages over planes parallel to walls.

Results are computed for a low Reynolds number of $Re_\tau = 180$ ($Re_B \approx 2{,}800$). The computational domain is $4\pi\delta$ by 2δ by $4\pi\delta/3$. The initial mesh of 33 $\times$ 65 $\times$ 33 nodes is comparable to that adopted by earlier researchers for this Reynolds number, although higher-order numerical methods have been used in most previous work (e.g., Piomelli 1993). Mesh spacing is uniform in x_1 and x_3 and follows a tanh distribution in x_2. Grid spacing varies from a minimum of $\Delta y^+ = 0.87$ at the wall to a maximum of $\Delta y^+ = 11.7$ at the channel centerline, where the $^+$ notation denotes standard wall-units scaling ($y^+ \equiv y u_\tau/\nu$). Computations are periodic in x_1 and x_3, with no-slip boundaries at $x_2 = 0$ and $x_2 = L_2$.

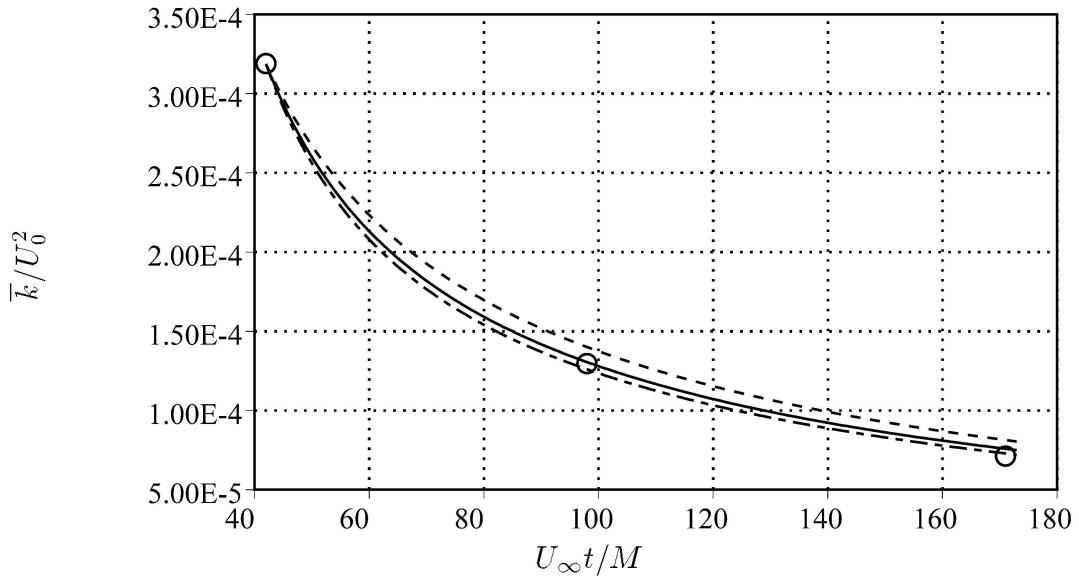

FIGURE 1. Decay of filtered turbulence kinetic energy for homogeneous isotropic decaying turbulence. Filter corresponds to a top-hat in physical space on a 32^3 uniform mesh with trapezoidal-rule integration. Symbols are measurements of Comte-Bellot & Corrsin (1971): ∘ . Lines are computations: ---- no subgrid-scale model; —-— constant-coefficient Smagorinsky model with $C_s = 0.17^2$; ——— dynamic Smagorinsky model.

Periodicity in the streamwise direction is maintained by imposing a streamwise body force g_1 (Eq. 1) consistent with the desired Re_τ. A global force balance in the x_1 direction yields,

$$g_1 = 2L_2^{-1}(\nu Re_\tau/\delta)^2 \ . \tag{17}$$

Fluid viscosity is set to maintain the desired bulk Reynolds number Re_B. Velocity and length scales are $U_0 = U_B$ and $L_0 = \delta$; remaining parameters are set according to Eq. (3). The flow is allowed to develop for about 20 flow-through times $t_{\rm dev}U_b/L_1 \approx 20$ ($t_{\rm dev}u_\tau/\delta \approx 15$). Profiles of mean velocity, Reynolds stresses, and other statistics as functions of x_2 then are accumulated by averaging over planes parallel to walls and over time using averaging times $t_{\rm avg}$ of at least $t_{\rm avg}u_\tau/\delta = 5$. Computed results are compared to DNS results of Kim *et al.* (1987) at the same Re_τ.

4.4 Axisymmetric piston-cylinder assembly

The target configuration for establishing the feasibility of in-cylinder LES is the simplified piston-cylinder assembly of Morse *et al.* (1978). There flow enters a pancake (flat head and piston) chamber through a central pipe of inside diameter 18.75 mm and length 1.8 m. The piston is driven in simple harmonic motion at a speed of 200 r/min through a 60-mm stroke; there is no compression. Bore diameter is 75-mm bore, and top-dead-center clearance height is 30-mm. Laser-Doppler anemometry has been used to obtain ensemble-mean (phase-averaged) radial profiles of mean and rms axial velocity at 10-mm axial increments starting at the

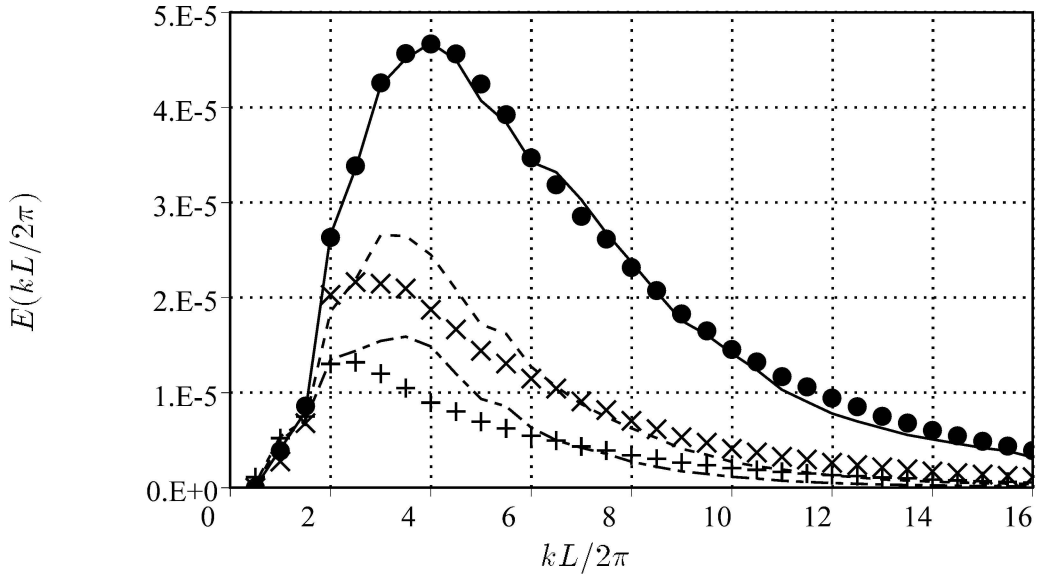

FIGURE 2. Evolution of filtered three-dimensional energy spectra for homogeneous isotropic decaying turbulence. The filter is a top-hat of width $2\pi/16$ in physical space with trapezoidal-rule integration. Symbols are experimental measurements of Comte-Bellot & Corrsin (1971): • $U_\infty t/M = 42$; × $U_\infty t/M = 98$; + $U_\infty t/M = 171$. Lines are computations for the constant-coefficient Smagorinsky model with $C_s = 0.17^2$ on 32^3 meshes: —— $U_\infty t/M = 42$; ---- $U_\infty t/M = 98$; —·— $U_\infty t/M = 171$.

head for crank positions of 36°, 90°, 144°, and 270° after top-dead-center. This flow can be thought of as an extension of the classic statistically stationary sudden expansion/contraction to a statistically periodic case.

Several pieces of information are sought from these computations. First, we can evaluate the performance of subgrid-scale turbulence models in a configuration approaching that of an engine on a deforming unstructured mesh. Second, we will build experience with explicit phase- (ensemble-) averaging compared to spatial filtering and traditional RANS modeling. Third, we can establish mesh resolution requirements, particularly in the vicinity of walls. This includes a determination of the need for explicit wall models beyond that provided by the subgrid-scale model. And fourth, we will explore the nature of inflow forcing required to generate realistic in-cylinder flow variability.

5. Results

All displayed results represent the resolved motion delivered by the numerical method in combination with the specified subgrid-scale model. These are the $\overline{()}$-filtered quantities as defined in Section 3. No attempt has been made to add explicit subgrid-scale contributions to the stresses.

5.1 Decay of homogeneous isotropic turbulence

The effect of filtering on the fraction of resolved turbulence kinetic energy in the experiments of Comte-Bellot & Corrsin (1971) has been computed. For the filtering

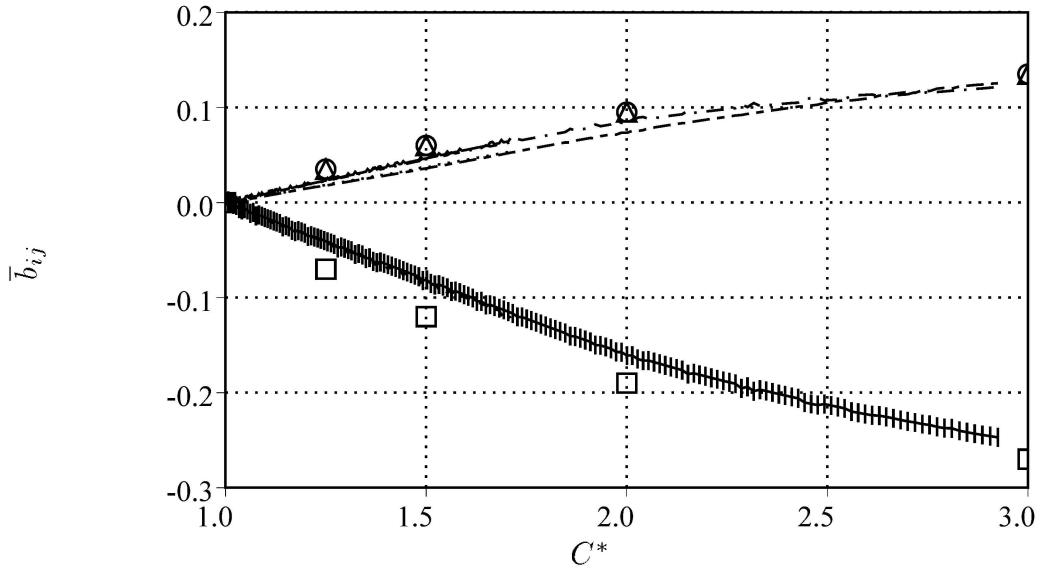

FIGURE 3. Evolution of the normalized anisotropy tensor $\overline{b}_{ij}$ as a function of total strain C^* for the linear expansion. Open symbols are RDT results (Kassinos & Reynolds 1994): ○ RDT, b_{11}; △ RDT, b_{22}; □ RDT, b_{33}. Lines are computations for the constant-coefficient Smagorinsky model with $C_s = 0.17^2$ on 32^3 meshes: ——— $S_{33} \cdot \overline{k}/\overline{\epsilon} \approx 4$, b_{11}; ····· $S_{33} \cdot \overline{k}/\overline{\epsilon} \approx 4$, b_{22}; - - - - $S_{33} \cdot \overline{k}/\overline{\epsilon} \approx 4$, b_{33}; —·— $S_{33} \cdot \overline{k}/\overline{\epsilon} \approx 8$, b_{11}; — - — $S_{33} \cdot \overline{k}/\overline{\epsilon} \approx 8$, b_{22}; +++++ $S_{33} \cdot \overline{k}/\overline{\epsilon} \approx 8$, b_{33}. (Results for the lower rate-of-strain S_{33} are indistinguishable from those at the higher S_{33}.)

assumed to be closest to our numerical method (top-hat filter with trapezoidal-rule integration) only about 45% of the energy is resolved at the first measurement station on the 32^3 mesh.

The decay of filtered turbulence kinetic energy versus time for the 32^3 mesh is displayed in Figure 1. With no subgrid-scale model, there already is substantial decay resulting mainly from numerical dissipation. Constant-coefficient Smagorinsky adds sufficient additional dissipation to yield good agreement with measurements, using the standard value of the model coefficient ($C_s = 0.17^2$). The dynamic Smagorinsky model yields similar results, returning a value of $C_s \approx 0.16^2$, close to the standard value.

Filtered three-dimensional energy spectra are plotted in Figure 2. There is a pile-up of energy at wave numbers just beyond the peak of the spectrum in the computations. Thus while we are able to match the energy decay rate on this coarse mesh, the dynamics of the system are not fully captured. This is not surprising in a computation where less than half of the energy is resolved.

5.2 Linear strain of initially isotropic turbulence

Evolution of the normalized anisotropy tensor as a function of total strain is given in Figs. 3 and 4. Results are presented for two different values of $S_{33} \cdot \overline{k}/\overline{\epsilon}$ to show the influence of mean rate-of-strain. All numerical results are for a 32^3 mesh using the constant-coefficient Smagorinsky model ($C_s = 0.17^2$). RDT data are shown for

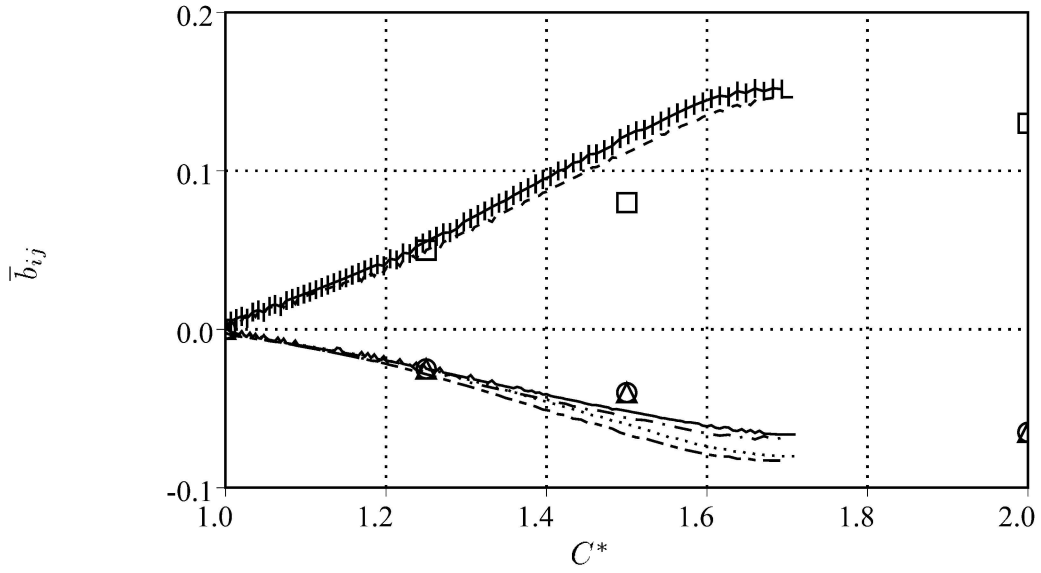

FIGURE 4. Evolution of the normalized anisotropy tensor $\overline{b}_{ij}$ as a function of total strain C^* for the linear compression. Open symbols are RDT results (Kassinos & Reynolds 1994): ○ RDT, b_{11}; △ RDT, b_{22}; □ RDT, b_{33}. Lines are computations for the constant-coefficient Smagorinsky model with $C_s = 0.17^2$ on 32^3 meshes: ——— $S_{33} \cdot \overline{k}/\overline{\epsilon} \approx -4$, b_{11}; ····· $S_{33} \cdot \overline{k}/\overline{\epsilon} \approx -4$, b_{22}; - - - - $S_{33} \cdot \overline{k}/\overline{\epsilon} \approx -4$, b_{33}; —·— $S_{33} \cdot \overline{k}/\overline{\epsilon} \approx -8$, b_{11}; —·· $S_{33} \cdot \overline{k}/\overline{\epsilon} \approx -8$, b_{22}; +++++ $S_{33} \cdot \overline{k}/\overline{\epsilon} \approx -8$, b_{33}.

comparison.

For the linear expansion, computations are in good quantitative agreement with RDT and are insensitive to the applied mean rate-of-strain (Fig. 3). This is consistent with experimental trends reviewed by Kassinos & Reynolds (1994).

Results for the linear compression warrant further discussion (Fig. 4). In this case computed results are closer to RDT for the slower mean rate-of-strain, and the degree of anisotropy increases with increasing mean rate-of-strain. This is contrary to experimental trends, which show increasing anisotropy at slower rates of strain (Kassinos & Reynolds 1994).

The Reynolds-averaged turbulence stress transport equation for homogeneous turbulence subjected to a uniform mean strain rate is derived by standard procedures,

$$\frac{d\big(\rho\langle\overline{u}'_k\overline{u}'_l\rangle\big)}{dt} = -\rho\langle\overline{u}'_i\overline{u}'_k\rangle\frac{\partial\langle\overline{u}_l\rangle}{\partial x_i} - \rho\langle\overline{u}'_i\overline{u}'_l\rangle\frac{\partial\langle\overline{u}_k\rangle}{\partial x_i} + \overline{T}^r_{kl} + \overline{T}^s_{kl} - \overline{\epsilon}_{kl}\ . \qquad (18)$$

The prime notation emphasizes that there is non-zero mean flow, $\overline{u}'_i \equiv \overline{u}_i - \langle\overline{u}_i\rangle$. Here the first two terms on the right-hand side represent the rate of production, $\overline{T}^r_{kl}$ and $\overline{T}^s_{kl}$ are the 'rapid' and 'slow' pressure-rates-of-strain, respectively, and $\overline{\epsilon}_{kl}$ is the viscous dissipation. In the limit of rapid distortion, $\overline{\epsilon}_{kl}$ and $\overline{T}^s_{kl}$ are negligible.

For the present linear mean strains, $\partial\langle\overline{u}_i\rangle/\partial x_j = S_{33}\delta_{i3}\delta_{j3}$. Thus all turbulence production goes directly into $\langle\overline{u}'^2_3\rangle$ and is redistributed to the other two components

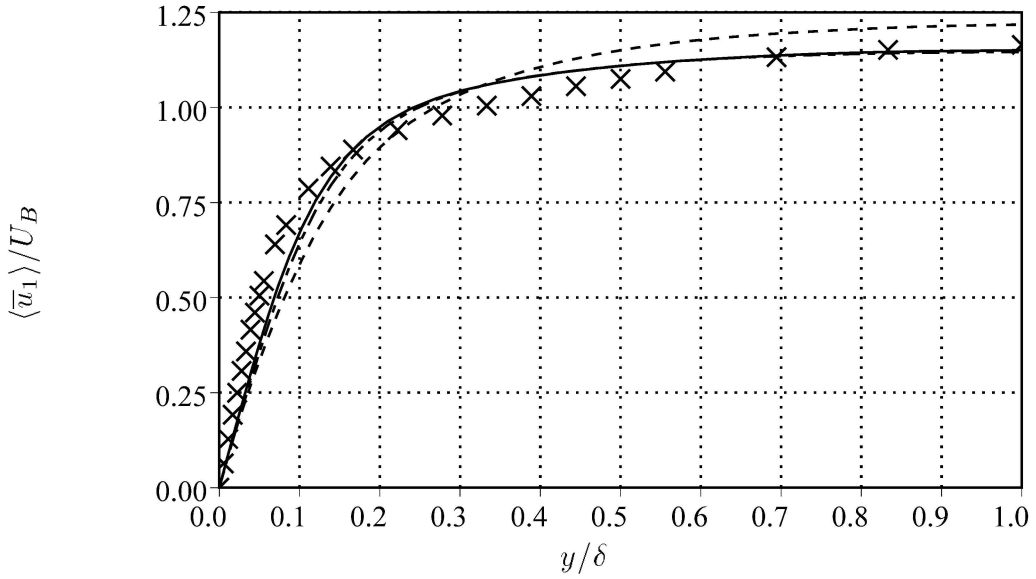

FIGURE 5. Streamwise mean velocity profiles normalized by the bulk velocity U_B for the planar channel flow at $Re_\tau = 180$. Symbols ($\times$) are the DNS data of Kim *et al.* (1987). Lines are computations on the $33\times65\times33$ mesh: ---- constant-coefficient Smagorinsky, $C_s = 0.17^2$; — - — dynamic Smagorinsky; ——— Lagrangian dynamic Smagorinsky.

$\langle\overline{u}_1'^2\rangle$ and $\langle\overline{u}_2'^2\rangle$ via the pressure-rate-of-strain terms. For the low-resolution LES computations of linear compression, the effective rapid pressure-rate-of-strain model does not redistribute sufficient energy from the 'direct' production component to the other two. Moreover, the effective slow pressure-rate-of-strain model responds incorrectly to a decrease in the mean rate-of-strain.

5.3 Planar channel flow

Mean velocity profiles from the dynamic Smagorinsky and Lagrangian dynamic Smagorinsky models are very similar to one another, and show better agreement with DNS than the constant-coefficient model (Fig. 5). All three models deviate from DNS in the logarithmic region ($y^+ > 10$). Ratios of centerline mean velocity to bulk velocity $\langle\overline{u}_1(y=\delta)\rangle/U_B$ are 1.22 for constant-coefficient Smagorinsky, 1.15 for dynamic Smagorinsky, 1.15 for Lagrangian dynamic Smagorinsky, and 1.16 for the DNS of Kim *et al.* (1987).

Both dynamic models effectively 'turn down' the subgrid-scale viscosity in the vicinity of the wall. The mesh spacing $\overline{\Delta}$ decreases close to the wall, as does the model coefficient C_s. The latter behavior is demonstrated in Fig. 6. There computed profiles of $C_s^{1/2}$ extracted from the dynamic model and the Lagrangian dynamic model are shown. For the former model, the standard value of 0.1 is recovered in the center of the flow, with a rapid drop-off to zero at the walls. The Lagrangian dynamic model behaves similarly out to a distance of about $y^+ \approx 40$, but levels off to a lower value of $C_s^{1/2} \approx 0.06$ at the centerline.

Computed Reynolds-stress profiles from the Lagrangian dynamic model are given

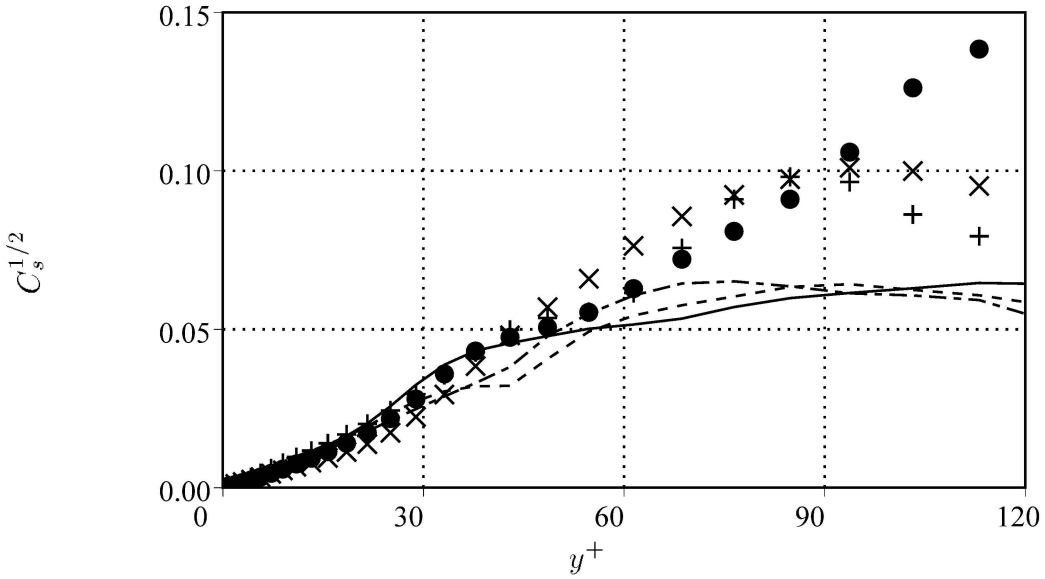

FIGURE 6. Computed profiles of $C_s^{1/2}$ adjacent to the lower wall for the planar channel flow at $Re_\tau = 180$. Symbols (• , × , +) are planar-averaged profiles from the dynamic Smagorinsky model at three instants of time. Lines (——— , - - - - , — - —) are planar-averaged profiles from the Lagrangian dynamic Smagorinsky model at three instants of time.

in Figs. 7 and 8. Results from the dynamic model are similar, while the constant-coefficient model yields somewhat poorer profiles (not shown). This is consistent with our findings from the mean velocity profiles of Fig. 5. Normal stress components display qualitatively correct behavior (Fig. 7), but there are significant quantitative departures from the DNS data. In particular, on this coarse mesh, all models tend to leave too much energy in the direct production component $\langle \overline{u}_1'^2 \rangle$ at the expense of $\langle \overline{u}_2'^2 \rangle$ and $\langle \overline{u}_3'^2 \rangle$. The value of the peak shear stress is computed reasonably well, although the LES profile is shifted outward from the wall compared to the DNS data (Fig. 8). These findings suggests that the present mesh resolution is marginal for computing second-order statistics, especially in the log-law region.

5.4 Axisymmetric piston-cylinder assembly

Computations are in progress at the time of this writing. Quantitative comparisons with measurements of Morse *et al.* (1978) are forthcoming.

6. Discussion and conclusions

This research has explored a candidate numerical methodology and subgrid-scale stress models for LES of flow in reciprocating IC engines. The present results have been obtained using coarse meshes that are representative of minimal mesh requirements for spectral LES. Generally reasonable evolution of first and second moments has been found nevertheless. This is an encouraging finding, given the low formal accuracy of the numerics. Based on these early results, it is anticipated that acceptable accuracy can be obtained using practical mesh densities.

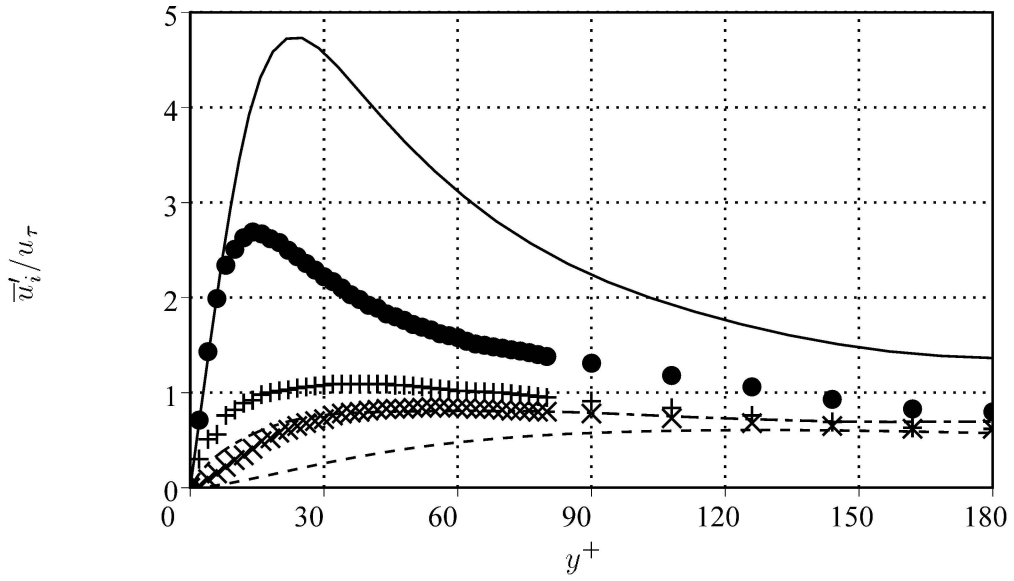

FIGURE 7. Turbulence intensities normalized by the wall friction velocity u_τ for the planar channel flow at $Re_\tau = 180$. Symbols are the DNS data of Kim *et al.* (1987): • streamwise (x_1) component; × wall-normal (x_2) component; + cross-stream (x_3) component. Lines are computations using the Lagrangian dynamic Smagorinsky model (resolved portion): ——— streamwise (x_1) component; - - - - wall-normal (x_2) component; —·— cross-stream (x_3) component.

Specific deficiencies have been attributed to inadequate spatial resolution. These include the energy spectrum decay for isotropic turbulence and insufficient energy transfer from the 'direct' production component for linear compression and planar channel flow. The two dynamic models have demonstrated an advantage compared to the constant-coefficient model in the planar channel flow. No specific deficiencies of the dynamic subgrid-scale models have been identified. In some cases, model results are not much different than those obtained in the absence of any explicit subgrid-scale model. This is consistent with earlier LES work for coarse meshes and low-order numerical methods. It remains to establish that these deficiencies can be overcome through mesh refinement, and to quantify resolution requirements for a specified level of fidelity to experiment or to benchmark computations. Short of explicitly filtering the governing equations at a scale much larger than the mesh spacing, it will remain difficult to isolate numerical inaccuracy from subgrid-scale model performance in LES.

Beyond spatial resolution, the most pressing outstanding issue is the lack of analytic characterization of the filtering implied by non-spectral numerical methods: what is $\overline{u}_i$? While it is straightforward to analyze and implement a variety of filters in spectral methods (e.g., spectral cutoff, spatial top-hat, spatial/spectral Gaussian), there has been little analysis to guide the implementation of filters implicit in finite-difference, finite-volume, or finite-element schemes on unstructured meshes. Our experience with the initial spectrum for decaying turbulence shows that the present discretization scheme affects all wavenumbers to some extent. The same has

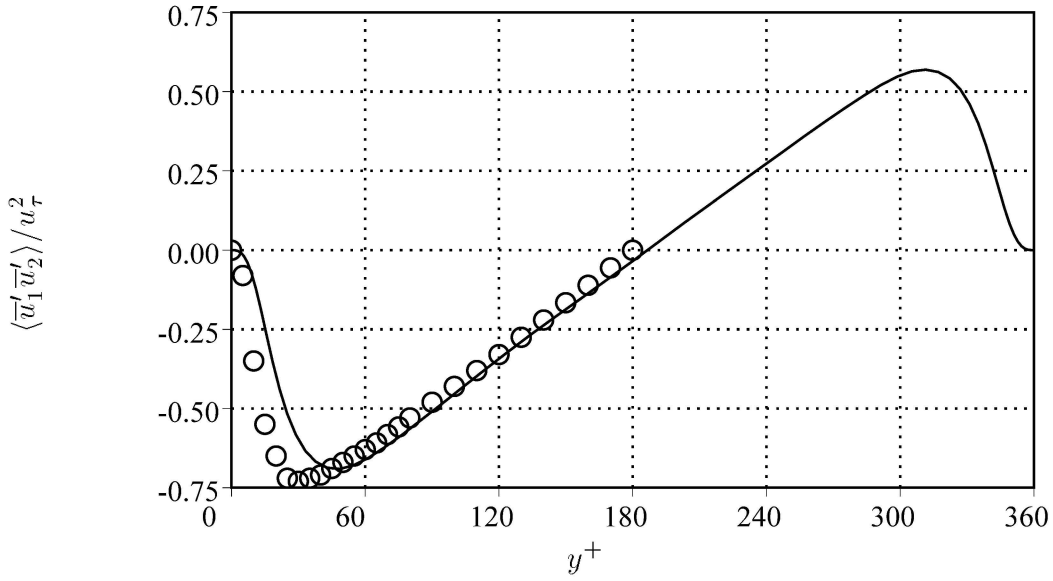

FIGURE 8. Turbulence shear stress normalized by the square of the wall friction velocity for the planar channel flow at $Re_\tau = 180$. Symbols ($\circ$) are the DNS data of Kim *et al.* (1987). Lines (———) are computations using the Lagrangian dynamic Smagorinsky model (resolved portion).

been found for other non-spectral methods that are being explored for unstructured LES (Jansen 1995).

Other outstanding issues for in-cylinder LES include wall treatment and inflow boundary conditions. Piomelli (1993) has shown that accurate LES results can be obtained using the dynamic model at high Reynolds numbers without further explicit wall modeling. The challenge at inflow boundaries is to establish the nature of forcing needed to yield in-cylinder velocity statistics representative of measured 'cyclic variability.' A final determination of suitability awaits the results of finer-mesh simulations for the three canonical configurations, and multiple-cycle results for the axisymmetric piston-cylinder assembly.

Acknowledgments

The first author thanks Drs. M. S. Sahota and P. J. O'Rourke of Los Alamos National Laboratory for many helpful discussions related to the use of CHAD. This project benefited immeasurably from the opportunity to interact with the other CTR Summer Program visitors and hosts. In particular, we thank Prof. Parviz Moin for the opportunity to participate.

REFERENCES

AMSDEN, A. A., O'ROURKE, P. J. & BUTLER, T. D. 1989 KIVA-II: a computer program for chemically reactive flows with sprays. *Los Alamos National Laboratory Report LA-11560-MS.*

COMTE-BELLOT, G. & CORRSIN, S. 1971 Simple Eulerian time correlation of full- and narrow-band velocity signals in grid-generated, 'isotropic' turbulence. *J. Fluid Mech.* **48,** 273-337.

EL TAHRY, S. H. & HAWORTH, D.C. 1992 Directions in turbulence modeling for in-cylinder flows in reciprocating IC engines. *AIAA J. Prop. & Power.* **8,** 1040-1048.

EL TAHRY, S. H. & HAWORTH, D.C. 1996 A perspective on the state-of-the-art in IC engine combustion modeling. *SIAM Sixth International Conference on Combustion, New Orleans, LA.* (To be submitted for publication.)

GERMANO, M., PIOMELLI, U., MOIN, P. & CABOT, W.H. 1991 A dynamic subgrid-scale eddy viscosity model. *Phys. Fluids A.* **3,** 1760-1765.

HAWORTH, D. C., EL TAHRY, S. H., HUEBLER, M. S. & CHANG, S. 1990 Multidimensional port-and-cylinder flow calculations for two- and four-valve-per-cylinder engines: influence of intake configuration on flow structure. *SAE Paper No. 900257.* (Also *SAE Trans., J. of Engines*, 1990.)

JANSEN, K. 1995 Preliminary large-eddy simulations of flow around a NACA 4412 airfoil using unstructured grids. *CTR Annual Research Briefs - 1995.* NASA Ames/Stanford Univ.,61-72.

KASSINOS, S. C. & REYNOLDS, W. C. 1994 A structure-based model for the rapid distortion of homogeneous turbulence. *Stanford University Dept. of Mech. Eng. Thermosciences Division Report TF-61.*

KIM, J., MOIN, P. & MOSER, R. 1987 Turbulence statistics in fully developed channel flow at low Reynolds number. *J. Fluid Mech.* **177,** 133-166.

LILLY, D.K. 1992 A proposed modification of the Germano subgrid-scale closure method. *Phys. Fluids A.* **4,** 633-635.

MENEVEAU, C., LUND, T. S. & CABOT, W. H. 1996 A Lagrangian dynamic subgrid-scale model of turbulence. *J. Fluid Mech.* **319,** 353-385.

MORSE, A. P., WHITELAW, J. H. & YIANNESKIS, M. 1978 Turbulent flow measurement by laser Doppler anemometry in a motored reciprocating engine. *Imperial College Dept. Mech. Eng. Report FS/78/24.*

O'ROURKE, P. J. & SAHOTA, M. S. 1996a A variable explicit/implicit numerical method for calculating advection on unstructured grids. (Submitted to *J. Comput. Phys.*)

O'ROURKE, P. J. & SAHOTA, M. S. 1996b NO-UTOPIA: the flow solver for the CHAD computer library. *Los Alamos National Laboratory Report.* (In preparation.)

PIOMELLI, U. 1993 High Reynolds number calculations using the dynamic subgrid-scale stress model. *Phys. Fluids A.* **5,** 1484-1490.